Cluster Dynamics with HETDEX at z < 0.5 - I: Simulated Performance, Mass Recovery, and Limits to Cosmology

Steven Boada,[1,2]⋆ C. Papovich,[2] R. Wechsler,[3,4] J. DeRose,[3] T. S. Li,[7] K. Gebhardt,[6] G. Hill,[6] E. Rozo,[3,5] E. S. Rykoff [3]

[1] *Physics and Astronomy Department, Rutgers University, Piscataway, NJ 08854-8019, USA*
[2] *George P. and Cynthia Woods Mitchell Institute for Fundamental Physics and Astronomy, and Department of Physics and Astronomy, Texas A&M University, College Station, TX, 77843-4242, USA*
[3] *Kavli Institute for Particle Astrophysics and Cosmology, Department of Physics, Stanford University, Stanford, CA 94305, USA*
[4] *Department of Particle Physics and Astrophysics, SLAC National Accelerator Laboratory, Menlo Park, CA 94025, USA*
[5] *Department of Physics, University of Arizona, Tucson, AZ 85721, USA*
[6] *Department of Astronomy, The University of Texas at Austin, Austin, TX 78712, USA*
[7] *Fermi National Accelerator Laboratory, P. O. Box 500, Batavia, IL 60510, USA*

ABSTRACT
The distribution of massive clusters of galaxies depends strongly on the total cosmic mass density, the mass variance, and the dark energy equation of state. As such, measures of galaxy clusters can provide constraints on these parameters and even test models of gravity, but only if observations of clusters can lead to accurate estimates of their total masses. Here, we carry out a study to investigate the ability of a blind spectroscopic survey to recover accurate galaxy cluster masses through their velocity dispersion using probability based and machine learning methods. We focus on the Hobby Eberly Telescope Dark Energy Experiment (HETDEX), which will employ new Visible Integral-Field Replicable Unit Spectrographs (VIRUS), over 420 degree^2 on the sky with a 1/4.5 fill factor. VIRUS covers the blue/optical portion of the spectrum ($3500 - 5500$ Å), allowing surveys to measure redshifts for a large sample of galaxies out to $z < 0.5$ based on their absorption features or [O II] $\lambda 3727$ emission (and Lyman-α over $1.9 < z < 3.5$). We use a detailed mock galaxy catalog from a semi-analytic model to simulate surveys observed with VIRUS, including: (1) a blind, HETDEX-like survey with an incomplete but uniform spectroscopic selection function; and (2) integral field unit surveys that target clusters directly, obtaining spectra of all galaxies in a VIRUS-sized field. For both surveys, we include realistic uncertainties from galaxy magnitude and line-flux limits. We benchmark both surveys against spectroscopic observations with "perfect" knowledge of galaxy line-of-sight velocities. With HETDEX, we can recover cluster masses to ~ 0.1 dex which can be further improved to < 0.1 dex with targeted follow-up observations. This level of cluster mass recovery enables independent constraints on σ_8 to $< 20\%$, and the unique properties of the observations will provide important calibrations for the zeropoint and scatter in the optical richness–mass relation.

1 INTRODUCTION

Our ability to perform precision cosmology with clusters of galaxies has reached a critical point. The widely accepted ΛCDM model of cosmology makes explicit predictions about the mass function of galaxy clusters in the universe. Measuring this mass function across many redshifts, in turn, provides constraints on the cosmology. Today, large-area sky surveys are providing observations of large numbers of clusters, but systematics in deriving cluster masses dominate the error budget (e.g., Sehgal et al. 2011; Planck Collaboration 2013; Bocquet et al. 2015). To place further constraints on the ΛCDM model of cosmology, we must decrease these systematics.

As mass is not a direct observable, a lot of work is underway to characterize galaxy cluster masses with an observable feature of galaxy clusters (e.g., Mantz et al. 2016; Bocquet et al. 2015; Old et al. 2015, 2014; Pearson et al. 2015). The goal is to constrain $P(M|z, \vec{x})$ the probability density (P) that a galaxy cluster of given mass (M), located at a specific redshift (z), determined using an observable parameter or parameters ($\vec{x}$). Generally, cluster mass calibrations are done in one of three ways, through simulations, direct or statistical calibration.

One could use various simulations to attempt to calibrate this observable-mass relation (e.g., Vanderlinde et al. 2010; Sehgal et al. 2011). However, the primary challenge

to this method is the incomplete understanding of the baryonic physics which take place in galaxy cluster environments. While there have been (and continue to be) many improvements in the accuracy and power of simulations it is doubtful that in the coming years they will reach the accuracy level required where the observable–mass relation is dominated only by statistics (Weinberg et al. 2013).

The second broad method is the direct calibration of cluster masses. This recipe has two distinct but not always independent tracks. The "direct" method uses observations of a relatively small set of clusters and then uses observable mass proxies, including X-ray temperatures and luminosities (e.g., Mantz et al. 2010; Rykoff et al. 2014), microwave observations (e.g., Vanderlinde et al. 2010; Sehgal et al. 2011), optical richness (e.g., Abell 1958; Rykoff et al. 2012) or weak lensing (WL; e.g. Rozo et al. 2010) as examples, which provide a "true" mass. This directly calibrates the observable-mass relation which is then applied to a much larger sample. The complications lie in that the "true" masses are, in fact, estimations, and the methods used to recover these cluster masses are subject to their own limitations. X-ray based cluster masses assume hydrostatic equilibrium (e.g., Mantz et al. 2015) which may only be valid for a very small number and range of cluster masses. The Sunyaev-Zel'dovich Effect (SZE; Sunyaev & Zeldovich 1972), which uses the up-scattering of cosmic microwave background (CMB) photons to estimate cluster masses, provides accurate estimations of mass, but the ability to detect low mass galaxy clusters is currently limited by technology (e.g., Carlstrom et al. 2002) and can also be effected by the properties of the intracluster medium (e.g., Pipino & Pierpaoli 2010). WL estimates are, in principle, correct in the mean, but they suffer from signal-to-noise requirements, limiting their usefulness in low mass clusters (where the lensing signal is particularly weak), and potentially suffer from line-of-sight effects as WL is sensitive to all mass along the line-of-sight. Virial mass estimators which determine the cluster mass based on the motions of the member galaxies (e.g., Ruel et al. 2014; Sifón et al. 2015) are promising in that it is a direct measurement of the depth of clusters potential well, but suffer from systematics due to cluster formation physics which disrupts the velocity field, such as cluster mergers (e.g., Evrard et al. 2008) and tidal stripping (e.g., Faltenbacher & Diemand 2006).

The statistical method of determining galaxy cluster mass relies not on direct measurements of individual clusters but the calibration of observables for the entire sample which correlate with cluster mass. One example is the spatial clustering of the galaxy clusters themselves (e.g., Baxter et al. 2016). See Weinberg et al. (2013) for a comprehensive review. In practice, it will be a combination of the three methods touched on that will provide the most reliable determination of cluster masses.

Large-area sky surveys, both on going and planned, are revolutionizing cluster cosmology using a large range of wavelengths. The South Pole Telescope (SPT; Carlstrom et al. 2011) and the Atacama Cosmology Telescope (ACT; Swetz et al. 2011) are discovering many clusters through the SZE. Optically, the on going Dark Energy Survey (DES; The Dark Energy Survey Collaboration 2005) and planned Large Synoptic Survey Telescope (LSST; LSST Dark Energy Science Collaboration 2012) will identify many thousands of clusters to much lower masses than is possible with SZE

measurements. However, regardless of the discovery method used, spectroscopic follow-up is needed to further constrain $P(M|z, \vec{x})$. This follow-up becomes increasing important to help constrain the scatter in the mass estimates of other methods, and provides an additional, independent check of the observable-mass relationship used. But as the cluster dataset grows to many tens of thousands of clusters individual follow-up becomes increasingly impractical. Therefore, large spectroscopic surveys are needed to more fully understand the observable-mass relation of clusters.

The Hobby Eberly Telescope Dark Energy eXperiment (HETDEX; Hill et al. 2008) will observe high-redshift large scale structures using cutting edge wide-field integral field unit (IFU) spectrographs. Designed to probe the evolution of the dark energy equation of state etched onto high redshift ($z > 2$) galaxies by the Baryon Acoustic Oscillations (BAO) (Eisenstein et al. 2005), the survey will observe two fields for a total of 420 degree^2 (300 degree^2, Spring field and 120 degree^2, Fall field). Tuned to find Lyα emitting (LAE) galaxies at $1.9 < z < 3.5$, HETDEX expects to find 800,000 LAEs, and more than one million [O II] emitting galaxies at $z < 0.5$ masquerading as high-redshift galaxies (Acquaviva et al. 2014).

While a large portion of the $\sim 10^6$ interloping lower redshift galaxies will be field (not associated with a bound structure) galaxies, the large area covered by HETDEX is expected to contain as many as 50 Virgo-sized (halo mass $> 10^{15}$ M$_\odot$) clusters at $z < 0.5$. The near-complete spectroscopic coverage allows an unprecedentedly detailed look at a very large number of clusters ranging from group scales to the very massive. In addition to the recovery of accurate dynamical masses, detailed investigations of the of dynamical state of the clusters is possible.

It is unclear how a blind spectroscopic survey with an IFU will effect the recovery of galaxy cluster dynamical properties. Unlike many previous large cluster surveys (e.g., Milvang-Jensen et al. 2008; Robotham et al. 2011; Sifón et al. 2015) which use multi-object spectrographs, the Visible Integral-Field Replicable Unit Spectrograph (VIRUS; Hill et al. 2012) used by HETDEX samples the sky in a uniform but sparse way which could exclude member galaxies which would otherwise be included. Secondly, it is not straightforward to use spectroscopic redshifts predominately from emission-line galaxies to interpret the kinematic and dynamical states of the clusters.

This work plans to address these concerns in the following ways. We create and evaluate a HETDEX like selection "function" of galaxies over a similarly large portion of the sky and use well adopted techniques to recover the dynamical properties, such as velocity dispersion and cluster mass. In addition to standard techniques of cluster mass estimation, we investigate probability based and machine learning based approaches of cluster mass prediction. We compare these results to a series of targeted galaxy cluster observations, where each member galaxy is assumed to be observed. Each of these observations use realistic uncertainties from galaxy magnitude and line-flux limits. These strategies will better allow future work to predict the number and types of galaxy clusters which should be observed with VIRUS during both the HETDEX survey portion and through targeted follow up observations.

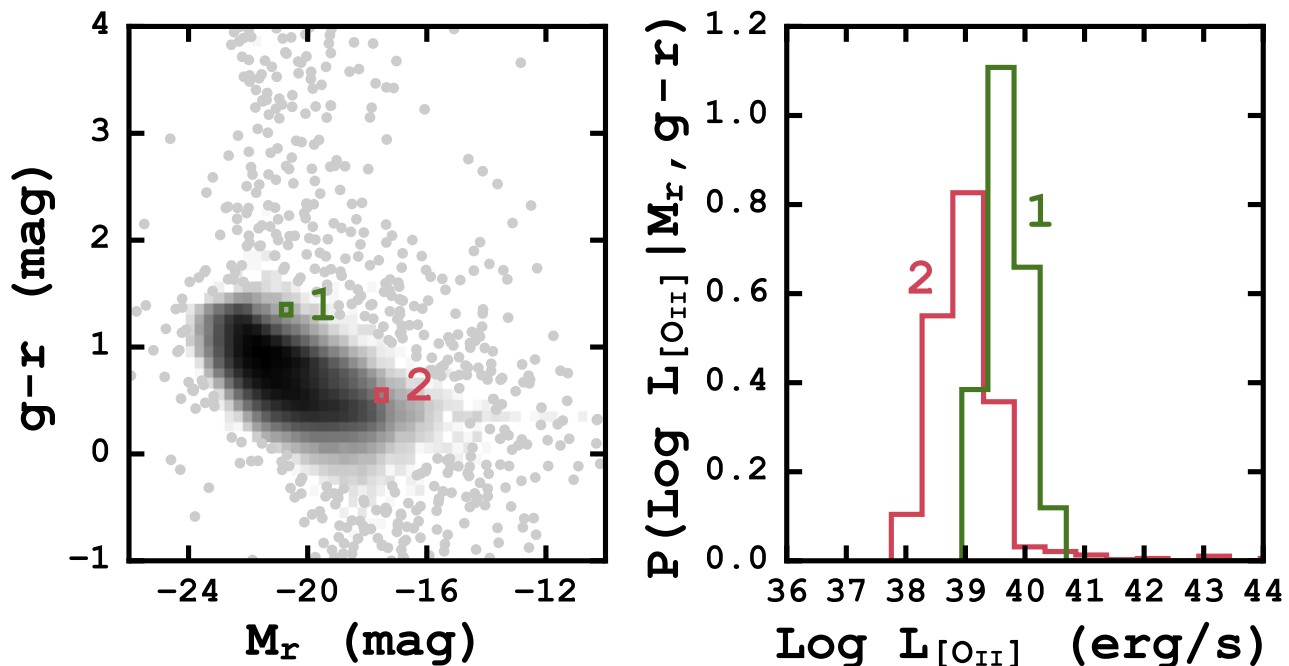We begin in Section 2 by giving an overview of what

Figure 1. *Left*: CMD of 503,113 $z < 0.2$ galaxies take from the SDSS DR12 where the shading scales with the density of points. The two colored boxes show regions containing potential catalog galaxies. *Right*: Probability histograms of the Log [O II] luminosity for the SDSS galaxies located in the two highlighted regions on the right. The [O II] luminosities are assigned to catalog galaxies from slice sampling the probability histogram and converted to fluxes using the redshift of each galaxy.

data is used, how it is created, and how we make our "observations." Details about the determination of cluster parameters, velocity dispersion, total mass, etc., are discussed in Section 3. Next, we present the results of our study in Section 4 and discuss their implications in Section 5. Finally we summarize our findings in Section 6. A follow-up to this work Boada et al. (in Preparation) will will apply these techniques to real data so as to empirically validate our conclusions.

Throughout this paper, we adopt the following cosmological model: $\Omega_\Lambda = 0.714$, $\Omega_M = 0.286$, $\sigma_8 = 0.82$ and $H_0 = 70$ km s^{-1}Mpc^{-1}(taken from the Buzzard catalogs; see below), assume a Chabrier initial mass function (IMF; Chabrier 2003), and use AB magnitudes (Oke 1974).

2 DATA AND MOCK OBSERVATIONS

In this section, we describe the data products and the techniques used to replicate the HETDEX survey. We use the information from a large mock galaxy catalog enhanced by the emission line properties of galaxies in the SDSS to create a realistic "sky" and "observe" it with a HETDEX-like observing strategy.

2.1 The Buzzard Mock Catalogs

The Buzzard mock galaxy catalogs provide a light cone covering 398.49 degree^2 between $4^h < RA < 6^h$ and $-61° < DEC < -41°$ and are derived from a combination of Sub-halo Abundance Matching (ShAM) and ADDSEDs

(Adding Density Dependent Spectral Energy Distributions) tied to an in house n-body cosmological simulation. A brief description of the catalog creation is described as follows. The initial conditions are generated with a second-order Lagrangian perturbation theory using 2LPTIC (Crocce et al. 2006). Dark matter (DM) n-body simulations are run using LGADGET-2 (a version of GADGET-2; Springel 2005). The Buzzard catalogs adopt the following cosmological parameters: $\Omega_m = 0.286$, $\Omega_\Lambda = 0.714$, $H_0 = 70$ km s^{-1}Mpc^{-1}, $\sigma_8 = 0.82$, and $n_s = 0.96$. The DM halos are identified using the ROCKSTAR halo finder (Behroozi et al. 2013) which also calculates halo masses.

Galaxy M_r luminosities are added to the velocity peaks using ShAM (Reddick et al. 2013), and ADDSEDs assign luminosities in the other bands. A M_r-density-SED relation is created using a SDSS training set, and for each mock galaxy the SED of a randomly selected training set galaxy which has a similar M_r and density is assigned. The assigned SED is also used to determine additional $ugiz$ magnitudes. The result is a mock catalog containing 238 million galaxies with $r < 29$ mag and $z \leq 8.7$.

The catalog information used in this study is broken into two large portions. The "truth" files contain the characteristics of each individual galaxy, such as right ascension (RA), declination (DEC), redshift (z), observed and rest-frame magnitudes, and many others. The "halo" files contain information for individual halos, to which many individual galaxies may belong. This includes estimations of dynamical mass, RA, DEC, z, three dimensional velocity dispersion, and many others. However, the catalogs do not include in-

formation for emission lines. We supplement the catalogs by generating this information; the process is described in Section 2.2.

We investigate the accuracy of the halo mass distribution by comparing the cumulative number density of halos above a mass (M_{200c}) threshold to the halo mass function (HMF) of Tinker et al. (2008). We calculate the HMF at central redshifts of 0.1, 0.2, and 0.4 using HMFCALC (Murray et al. 2013) and compare it to galaxy clusters in a redshift window of $\Delta z \pm 0.01$. We find a very good agreement between the predicted HMF and the observed distribution of clusters.

2.2 Conditional [O II] Flux Probability Distribution Functions

We use the SDSS DR12 (Alam et al. 2015) catalogs to assign [O II] emission line strengths to the galaxies in the Buzzard catalog. We use 503,113 objects classified as galaxies selected over $z = 0.02 - 0.2$ with ZWARNING = 0 and a measured [O II] line flux signal-to-noise of at least five. Figure 1 shows the color-magnitude diagram (CMD) of M_r and $g - r$ for these galaxies, and the following SQL query selects the appropriate galaxies:

```
SELECT  GAL.objid,
        GAL.u,
        GAL.err_u,
        GAL.g,
        GAl.err_g,
        GAL.r,
        GAL.err_r,
        GAL.i,
        GAl.err_i,
        GAL.z,
        GAL.err_z,
        g.oii_3726_flux,
        g.oii_3726_flux_err,
        s.z
FROM    galaxy AS GAL
        JOIN specobj AS s
          ON s.bestobjid = GAL.objid
        JOIN galspecline AS g
          ON g.specobjid = s.specobjid
WHERE   oii_3726_flux > oii_3726_flux_err * 5
        AND oii_3726_flux_err > 0
        AND s.class = 'GALAXY'
        AND s.zwarning = 0
```

To assign an [O II] luminosity to each galaxy in our catalog, we place the catalog galaxies on the same CMD and select all SDSS galaxies in a small 2D (M_r, $g - r$) bin around the galaxy. We extract all of the SDSS galaxies inside that bin and create a histogram of their [O II] luminosities, the right panel of Figure 1. Using a slice sampling technique (Neal 1997) we assign the catalog galaxy an [O II] luminosity based on the distribution of SDSS galaxies in that bin. In very few cases (1.3% of galaxies), the $g - r$ and M_r magnitudes of the galaxies in the Buzzard catalog do not overlap with the distributions in SDSS. For these objects, we assign them zero [O II] flux, but this has no impact on our analysis. For catalog galaxies with have very few ($1 \leq N < 10$) SDSS
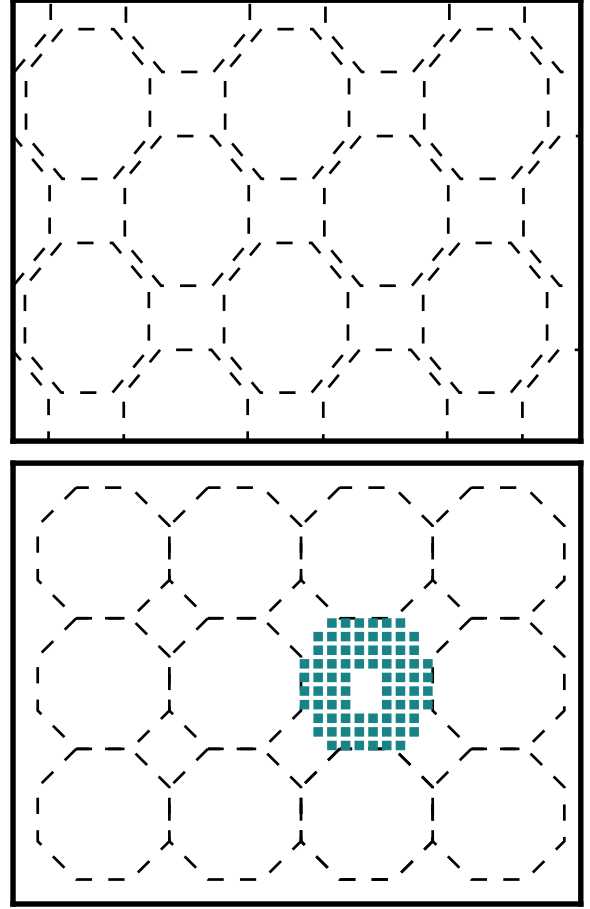

Figure 2. *Top:* Representative observation tiling scheme for the HETDEX $16' \times 16'$ pointings over a small region of the sky. *Bottom:* The simplified tiling pattern used in this study. In both schemes, the dashed octagons approximate the size of a single observation. Each observation consists of the 78 VIRUS IFUs, represented by the turquoise squares in the bottom panel shown for one of the HETDEX pointings. Inside each IFU HETDEX will achieve near complete coverage through three dithers. See the text for more details.

galaxies in their respective bin, we assign it the mean [O II] flux.

Figure 1 illustrates this process. The numbered boxes in the left panel show the bins corresponding to two example Buzzard galaxies ($M_r, g - r = -17.7$, 0.49 and $M_r, g - r = -21.4$, 1.24). The right panel shows the [O II] luminosity distribution functions, $P(\log L_{[O II]}|M_r, g - r)$, which we use to assign [O II] luminosity to each object. The luminosity is then converted into an [O II] flux through

$$F = \frac{L}{4\pi D_L^2} \tag{1}$$

where D_L is the luminosity distance (e.g., Hogg 1999).

2.3 HETDEX

We designed the results of this study to be used in conjunction with HETDEX, a large, blind, spectroscopic survey.

HETDEX will measure the redshifts of 8×10^5 LAE galaxies between $1.9 < z < 3.5$ using a collection of 78 wide-field IFU spectrographs covering the wavelength region $3500 - 5500$ Å at R ~ 750 (Hill et al. 2008). The primary science goal of these observations is to provide $< 1\%$ accuracy measurements of the Hubble expansion parameter and the angular diameter distance at $z \sim 2$. This result will provide significant constraints on the evolution of the dark energy equation of state which is both competitive with, and independent of, constraints derived from observations of the Lyα forest.

The entire HETDEX survey will cover 420 degree^2 with a 1/4.5 filling factor over two fields: a ~ 300 degree^2 northern field, and a ~ 140 degree^2 equatorial region. The spectral coverage allows for the detection of [O II] ($\lambda\lambda 3727, 3729$) emitters to $z \sim 0.5$ and Ca H ($\lambda 3968.5$) and K ($\lambda 3933.7$) absorption features to $z \sim 0.4$. The 10σ detection threshold for emission spectral features will be 3.5×10^{-17} erg s^{-1} cm^{-2} at 5000 Å, or equivalently, $g = 21.9$ mag for continuum objects.

The HETDEX IFU pattern is illustrated in Figure 2 by the turquoise squares. Each of the 78 IFUs, are comprised of 448 optical fibers subtending a $50'' \times 50''$ region on the sky (Kelz et al. 2014). The inter-IFU spacing is also $50''$, spanning a total area of $16' \times 16'$ on the sky. The individual IFUs have a fill-factor of 1/3, which will be completely filled with three dithers of the telescope at each pointing.

2.4 Mock Observations

When selecting galaxies from the Buzzard catalog we assume an observation for all galaxies laying within a turquoise, IFU square in Figure 2. In practice, this is achieved by three dither positions at each pointing. Because of the 1:3 fill factor, many galaxies will not receive spectroscopic coverage, including galaxies that lie between IFUs within a pointing, as well as galaxies between pointings. We use a pointing pattern which differs slightly from the expected final HETDEX observing pattern. See Figure 2 for an illustration of the difference. To cover the 398.49 degree^2 field of the Buzzard catalog we require 5370 pointings where 0.015 degree^2 of each pointing is covered by an IFU. The total area of the sky covered by an IFU is 80.80 degree^2 which gives a filling factor of 1/4.65, slightly (about 3%) decreased from the expected filling factor of 1/4.5.

We measure cluster velocity dispersions using three different spectroscopic observing patterns. We consider three separate observing strategies, Targeted, Survey and Perfect. The Targeted observations use "direct" observations where each cluster is targeted individually with a 1:1 fill factor such that every cluster member galxay is assumed to be observed. The Survey observations mimic the HETDEX observation pattern across the sky, where no cluster is directly targeted. Each cluster is observed with the 1/4.5 fill factor, such that not all cluster member galaxies are observed. Both of these observations have HETDEX-like galaxy detection thresholds (described in the previous subsection), so while a galaxy may be observed, a redshift will only be measured if the galaxy satisfies the continuum brightness or emission line flux limits for the HETDEX survey. For comparison we also include a Perfect observation, in which we assume all galaxies in a field are observed and all redshifts measured. This provides a baseline where the cluster velocity dispersion is calculated

under the best possible conditions and against which we can compare the results of the "Targeted" and "Survey" observing strategies.

3 RECOVERY OF PARAMETERS

In the following sections, we assume that we know *a priori* which galaxies belong to each individual cluster. So while our observations may include many field galaxies which do not belong to the cluster in question, we exclude those galaxies during the analysis of the cluster parameters. Cluster membership is a critical issue which must be addressed when utilizing real observations. To that end, we assay a small sample of real galaxy clusters in a follow up work (Boada et al. in Preparation).

3.1 Cluster Redshift

The accurate determination of the cluster redshift (z_c) is crucial to the reliability of all following measurements. An incorrect cluster redshift introduces error into the measured line-of-sight velocity (LOSV) and corresponding dispersion, which, in turn, contributes to errors associated with dynamical mass and radius.

In simple terms, the cluster redshift is the mean of the redshifts of all galaxies associated with the cluster, where the mean is the first moment of the velocity (redshift) distribution function $P(z)$. In practice, the first moment is strongly subject to outliers, so we rely instead on the biweight location estimator (Beers et al. 1990) through[1]:

$$z_c = z_{med} + \frac{\sum_{|u_i|<1}(z_i - M)(1 - u_i^2)^2}{\sum_{|u_i|<1}(1 - u_i^2)^2} \quad (2)$$

where z_i are the individual redshifts, z_{med} is the median redshift and u_i is given by:

$$u_i = \frac{(z_i - M)}{C\,\mathrm{MAD}}. \quad (3)$$

MAD is the median absolute deviation, also defined in Beers et al. (1990), and C is the a tuning constant. We choose $C = 6$ (the Beers et al. 1990 suggested value).

3.2 Line-of-Sight Velocity Dispersion

We calculate the LOSV, v_i, to each galaxy, where

$$v_i = c\frac{z - z_c}{1 + z_c} \quad (4)$$

and c is the speed of light, z is the redshift of the individual galaxy, and z_c is the overall cluster redshift described in the previous subsection.

We follow the maximum likelihood method of Walker et al. (2006) to estimate the line-of-sight velocity dispersion (LOSVD). Using the previously calculated LOSVs (v_i in the

---

[1] Implemented as part of the ASTLIB Python library (Hilton & Boada 2016). See http://astlib.sourceforge.net

following discussion), we maximize the probability function:

$$P(\{v_1, ..., v_N\}) = \prod_{i=1}^{N} \frac{1}{\sqrt{2\pi(\sigma_i^2 + \sigma_{1D}^2)}} \exp\left[-\frac{1}{2}\frac{(v_i - \langle u \rangle)^2}{(\sigma_i^2 + \sigma_{1D}^2)}\right] \tag{5}$$

where σ_{1D}, $\langle u \rangle$, and σ_i is the LOSVD, the average radial velocity and the error (which we have assumed to be normally distributed) on the individual v_i measurements respectively. To maximize Equation 5, we employ a Monte Carlo Markov Chain (MCMC) sampler (EMCEE[2]; Foreman-Mackey et al. 2013) which is based on affine-invariant ensemble sampler (see Goodman & Weare 2010 for details on affine-invariant samplers). We draw twenty thousand samples from the posterior probability distribution using simple priors, $\langle \mu \rangle$ lies between the maximum and minimum LOSV and $0 < \sigma_{1D} < 1400$ km s^{-1}, for each cluster. We set the upper limit on the LOSVD as the LOSVD corresponding to a 10^{16} M$_\odot$ cluster at $z \sim 0.0$, higher mass than any expected cluster in the Buzzard catalogs. When the complete sampling of the posterior probability distribution is not used, the final LOSVD is quoted as the median value of the posterior probability distribution with 68% error bars defined as the square root of second moment of the same distribution, the standard deviation.

In principle, a single statistic such as the biweight scale estimator or the gapper estimator (both from Beers et al. 1990) with many bootstrap resamplings could be used to construct a distribution of σ_{1D}. In simple tests where the values of both σ_{1D} and $\langle \mu \rangle$ are known, the 68% error bars derived from the MCMC method give slightly better results with the true LOSVD value bracketed by the error bars in $\sim 68\%$ of the cases versus $\sim 57\%$ with bootstrapping and a single statistic. In addition, we prefer the maximum likelihood method for its straight forward treatment of the errors in the LOSV measurements, which will become important in the practical application to real data (e.g., Boada et al. in Preparation).

3.3 Estimates of Cluster Mass

3.3.1 *Power Law Based Method*

The relationship between the LOSVD and cluster dynamical mass has been the focus of several previous works (e.g., Evrard et al. 2008; Saro et al. 2013; Sifón et al. 2013; van der Burg et al. 2014), where the relationship for the mass enclosed by r_{200c} takes the form

$$M_{200c} = \frac{10^{15}}{h(z)}\left(\frac{\sigma_{1D}}{A_{1D}}\right)^{1/\alpha} M_\odot \tag{6}$$

with $A_{1D} = 1177 \pm 4.2$ km s^{-1} (Munari et al. 2013; referred to as σ_{15} in Evrard et al. 2008 and other works), $\alpha = 1/3$, $h(z) = H(z)/100$ km s^{-1} Mpc^{-1}, and σ_{1D} is the LOSVD of the velocity tracers (dark matter particles, subhalos or galaxies). $H(z) = H_0 E(z)$ and $E(z) = \sqrt{\Omega_m(1 + z^3) + \Omega_\Lambda}$ (assuming a flat cosmology).

Recent work suggests that there is a significant difference in the observed LOSVD depending on the velocity tracers used (Munari et al. 2013). Specifically, while there is little difference between using galaxies and their host DM subhalos, there is a significant over estimation of the LOSVD when using galaxies/subhalos compared to DM particles. We follow other works (e.g., Kirk et al. 2015; Sifón et al. 2016) using the scaling relation, given in Equation 6 to facilitate comparisons with other observational studies, which rely on galaxies as tracers.

3.3.2 *Other Estimates of Dynamical Mass – Introduction*

In the following subsections we use two methods to predict the mass of a cluster based on other observables. Often the cluster mass is estimated based on a single observable, e.g. X-ray temperature, LOSVD, richness and others (see Section 1 for referenced examples). Here we combine many observables to attempt to correct the mass inferred solely from the velocity dispersion. The first method is traditional "probability based" where we marginalize over a series of observables to find the most probable cluster mass. The second is based on a machine learning (ML) algorithm which attempts to infer the relationship between the observables and the desired output, the cluster mass. Both of these methods are examples of supervised learning algorithms where the relationship between the observable parameters and the target parameter (the cluster mass) are both known.

As with any predictive analysis it is important to test the model on data that the model has not seen before. This prevents over-fitting. In the following subsections we take all of the simulated cluster observations, split them, and generate a *training* and *testing* set (e.g., Ripley 2007; Xu et al. 2013; Ntampaka et al. 2015, 2016; Acquaviva 2016). Traditionally, the training set is a set of data used to infer possibly predictive relationships. The test set of data is then used to assess the correctness of the predictive relationship. Our simulated observations are randomly split into 70% training and 30% testing. We follow the ML convention and refer to the individual clusters in each set as a "sample", and the parameters associated with the cluster (z, LOSVD, mass, etc.) as "features".

3.3.3 *Probability Based*

For internal consistency between this and the ML based method we use 70% of the clusters to establish a conditional probability density of $P(\log M_{200c}|\vec{x})$ which we then use as the cluster mass probability density for the remaining clusters with similar features. In this way we, "train" the probability density using the existing simulated data, and apply it to the "test" sample (the remaining 30% of the data not used as the training set).

In this method, the cluster masses are predicted using the method illustrated in Figure 3. The left panel shows the two dimensional (joint probability) projections of the posterior probability distributions of the feature training data. The conditional probability of the cluster mass $P(\log M_{200c}|\vec{x} = \{x_1, x_2, ...\})$ (shown in the right panel) is determined by selecting a region in the joint probability distribution. For example, using the LOSVD and red-
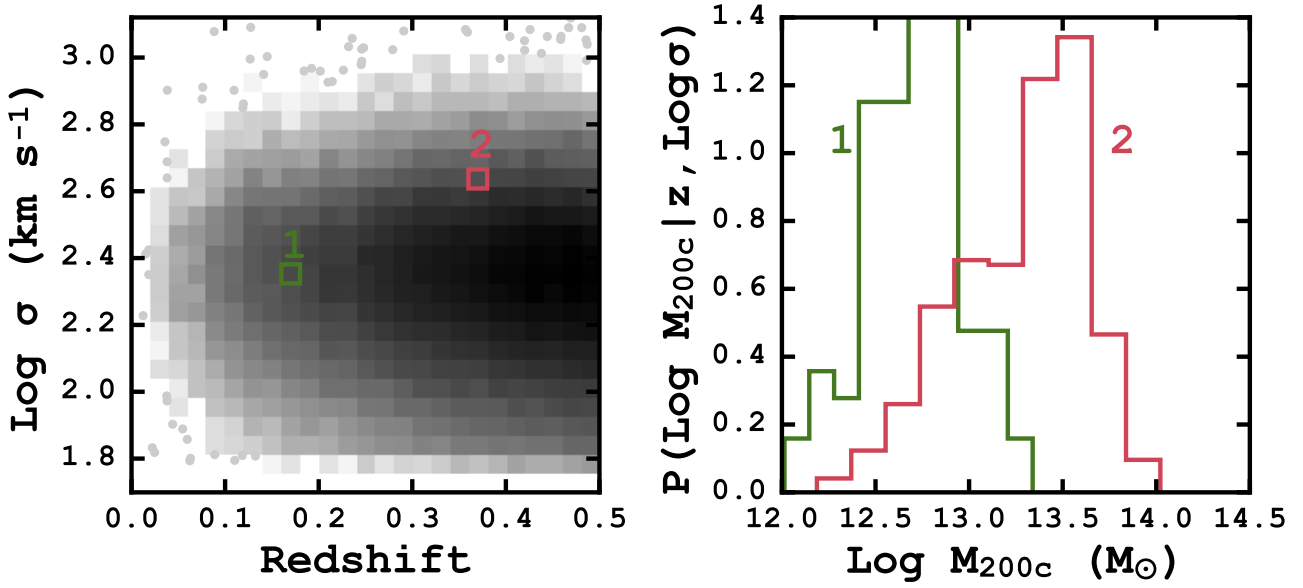
Figure 3. Illustration of the probability based cluster mass prediction method. *Left*: The two dimensional posterior probability distribution of LOSVD and redshift used to determine the correct cluster mass. The pink and green rectangles show the locations of two example galaxy, $\vec{x}_1 = \{z = 0.16, \log \sigma = 2.4\}$ and $\vec{x}_2 = \{z = 0.36, \log \sigma = 2.7\}$, clusters used to create the conditional probability distribution of the mass, $P(\log M_{200c}|z, \text{Log}\,\sigma)$. *Right*: The conditional probability distribution of the cluster mass for the two example galaxies. See text for a complete description.

shift features we create $P(\log M_{200c}|\vec{x})$ for two test galaxies, shown by the green and pink boxes in the left panel of Figure 3. These example galaxies have features $\vec{x} = \{\sigma = 200\,\text{km s}^{-1}, z = 0.16\}$ and $\vec{x} = \{\sigma = 400\,\text{km s}^{-1}, z = 0.36\}$. We select all galaxies in our training sample with similar features and create the conditional probability distributions shown in the right panel.

For the clusters making up the *test* sample the mass is unknown (it is what we are trying to predict) but the other features are known. To determine the mass probability distribution of a test cluster, $P(\log M_{200c})$, we combine the conditional probability distribution, $P(\log M_{200c}|\vec{x})$, created previously with the probability distribution of σ, the LOSVD, through Equation 7.

$$P(\log M_{200c}) = \int P(\log M_{200c}|\vec{x}) \, P(\log \sigma, z) \, d\log \sigma \, dz \tag{7}$$

The expected mass is determined by calculating the first moment of the probability density. This becomes our "predicted" cluster mass, M_{pred}.

$$\log M_{pred} = \int \log M_{200c} \, P(\log M_{200c}) \, d\log M_{200c} \tag{8}$$

The confidence interval associated with this prediction can be estimated two ways. First, by calculating the second moment of the probability density through

$$\text{Var} = \int (\log M_{200c} - \log M_{pred})^2 \, P(\log M_{200c}) \, d\log M_{200c} \tag{9}$$

or by drawing many samples from $P(\log M_{200c})$ and calculating the values at the 16th and 84th percentile. In practice

we find that both methods produce similar results for a large number of trials. Therefore, we quote predicted masses as the most probable mass given by Equation 8 and associated 68% error estimated through the square root of Equation 9.

3.3.4 Machine Learning Based

The cluster mass estimation in this section relies on a ML technique known as an ensemble method, where many estimators are created by a single learning method with the goal of improved generalization and robustness compared to a single estimation. Ensemble methods (e.g., Caruana & Niculescu-Mizil 2006) come in two general flavors. Averaging methods average (hence the name) the estimators to produce a single prediction. Boosting estimators build estimates sequentially by attempting to address poor performing estimators in each previous step, hence "boosting" the predictive power.

Here we use an averaging ensemble learning method known as a forest of randomized decision trees, often shorten to just random forest (RF; Tin Kam Ho 1995, 1998). Decision trees can be visualized a flow chart where forks are the branches of the tree. The path along the tree is decided by the values of the feature(s) at each branch. RF estimators use a random subset of the training set at each fork to decide which path should be followed. The final prediction is then the mean of all the final predictions from the trees. We use RF regression methods as implemented in SCIKIT-LEARN (Pedregosa et al. 2012).

The ML method generates "prediction intervals" between observed and derived quantities (rather than "confidence intervals"). A prediction interval is an estimate of

the interval encompassing future observations, with a certain probability. And, unlike confidence intervals, which describe uncertainties on the different moments of a population, a prediction interval is unique to each prediction. In many regresson analyses, such as linear fitting, the prediction intervals are based on underlying assumptions of normally distributed residuals. However, RF estimators do not have any such assumptions and require special treatment.

The prediction intervals here are based on the general method of quantile regression forests (Meinshausen 2006). The general idea is that all response variables are recorded, not just the mean. Then the prediction can be returned as the full conditional probability distribution of all responses, which allows us to generate the prediction intervals. We report the 68% prediction interval as the square root of the second moment of the full conditional probability distribution.

4   RESULTS

Here we explore the cluster member recovery rate and mass estimates for the two observing strategies, Targeted, and Survey. Targeted observations are direct observations of a cluster where each cluster member galaxy, above the detection thresholds (see Section 2.4), is observed. Survey observations mimic the HETDEX observation strategy such that no cluster is directly observed, and only the cluster member galaxies above the detection threshold and within an IFU (see Figure 2) are observed. We discuss the accuracy of cluster dynamical mass derived from both the power law scaling relation (see Equation 6) and through the probability and ML methods. We also compare the results from the Targeted and Survey observing strategies to the results of a "Perfect" survey, where the redshift of each galaxy, regardless of observational limits, in the cluster is known perfectly.

4.1   Recovery of Cluster Members

As discussed in Section 2.4, the observational constraints place limits on the total number of clusters member galaxies expected to be recovered. Knowing these limits will provide important information for potential future follow up or Targeted observations. We recover 14,189 clusters with Targeted observations and 1,760 clusters with Survey observations, where we require a detection of $N_{obs} >= 5$ galaxies for a cluster to be detected. It is worth noting that we are using galaxies which are a priori known to belong to each cluster. This is not possible to do when analyzing real data, but this will be investigated in a follow up paper, Boada et al. (in Preparation).

Figure 4 shows the recovery fraction of member galaxies, the number of observed galaxies divided by the number of actual galaxies (N_{obs}/N_{True}), as a function of both redshift and cluster mass. As expected, the Targeted observing strategy where the individual clusters are targeted through several dithers to ensure near complete coverage, performs significantly better than the Survey observing strategy across all redshifts and cluster masses. By definition, with Perfect knowledge, recovery fraction would be unity across all redshifts and cluster masses where clusters exist.

For the Targeted observations, shown in the left panel

of Figure 4, the pattern of decreasing recovery fraction as a function of redshift (y-direction) is due to the observational limits imposed. Because the redshift success rate of HETDEX is limited by apparent magnitude, we expect to recover fewer galaxies at higher redshift, where the galaxies are often below our 5σ detection threshold. For example, we tested this by constructing an artificial HETDEX-like survey, limited by volume for all galaxies with $M_g < -11$. In this case, our recovery fraction increases to $> 70\%$, which shows that the flux limit is dominating the (lower) recovery of our flux-limited survey.

For the recovery fraction as a function of true cluster mass (x-direction), we find a general decrease in the recovery fraction of member galaxies with increasing cluster mass. This is entirely a result of the flux limited survey (see previous paragraph). Because there are few high mass ($M_{200c} > 5 \times 10^{14}$ M$_\odot$) clusters, many of which are at moderately high redshift, the higher redshift cluster members suffer from the limiting apparent magnitude and suppress the recovery fraction at fixed mass. If we were to limit the Survey to $z < 0.2$ we find the recovery fraction of clusters, across all masses, increases substantially, and we find a much more consistent detection fraction across all masses. However, doing so limits severely the number of clusters at masses greater than 10^{14} M$_\odot$.

For the Survey observations, the right panel of Figure 4, all of the same effects are at work. In addition we find that the fill factor, due to the gaps between the VIRUS IFUs, further reduces the number of cluster members detected. The median recovery fraction in Survey observations is almost exactly 4.5 times less than the Targeted median recovery fraction. As the total filling factor of the Survey observations increases the two lines will converge.

The recovery fractions in Figure 4 are an outcome of the magnitude limit and [O II] line-flux limit of the survey. For Perfect observations, we would detect all members across all cluster masses and redshifts. Recovery fractions of clusters located a the low end of the redshift distribution will improve the most by follow-up targeted observations. But generally, the number of members observed (and subsequently more accurate cluster mass estimates) will benefit from follow-up observations regardless of the redshift. So follow-up observations should be tailored to the specific science goal.

4.2   Mass estimates

In this section we discuss the accuracy of the recovered masses compared to the true cluster mass from a set of observations. We report on three methods, the power law based approach (Eq. 6), the probability based approach (Section 3.3.3) and the ML based method (Section 3.3.4). For each method we consider observations with Perfect knowledge, Targeted observations and Survey observations.

Because it represents the best possible scenario, the Perfect knowledge observations should serve as a baseline to compare the power law based, probability based and ML cluster mass recovery methods. And, while there are many possible metrics to evaluate performance, we compute two: the average bias (given in Table 1)

$$\mu_{\text{bias}}(y, y_{pred}) = \frac{1}{N} \sum_{i=1}^{N} (y_{pred,i} - y_i). \quad (10)$$
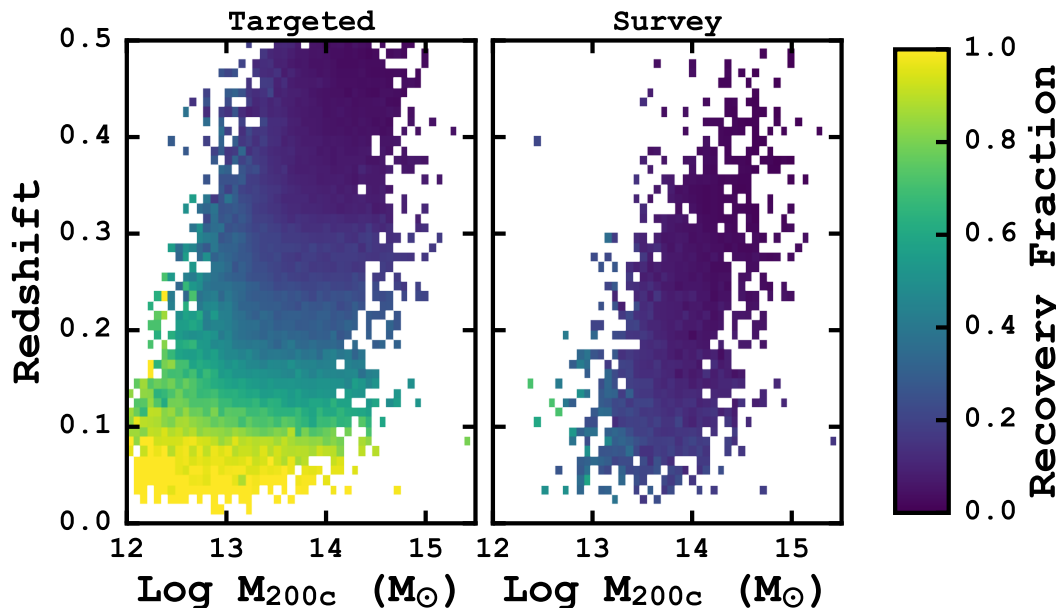
Figure 4. Recovery fractions (N_{obs}/N_{True}) of cluster member galaxies as a function of redshift and true cluster mass for the Targeted and Survey observing strategies. We have applied HETDEX-like observational limits on the cluster galaxy detection, and require at least five galaxies to be detected for a cluster to be recovered. The shading indicates the mean recovery fraction for clusters within each small bin of redshift and cluster mass. We find a significant decrease in the recovery of galaxies with increasing redshift. This leads to lower recovery fractions of high mass clusters as many only exist at larger redshifts. The significant decline in the number of galaxies observed with the Survey strategy is due to gaps in the VIRUS IFU, where the galaxies are missed.

where y are the true values and y_{pred} are the predicted values, and the scatter about the bias (given in Table 2)

$$\sigma_{bias}(y, y_{pred}, \mu_{bias}) = \left[\frac{1}{N-1} \sum_{i=1}^{N} (y_{pred,i} - y_i - \mu_{bias})^2 \right]^{1/2} \tag{11}$$

with N clusters in a given bin. Both metrics evaluate how closely the ensemble of predicted cluster masses are to the true cluster masses.

We begin with the Perfect knowledge observations. These observations are of the same clusters as the Targeted observations but without any observational limits. The cluster masses predicted by Equation 6 gives the following results. For clusters with masses between Log M/M$_\odot$ = 13 − 15.5, we find $\mu_{bias} = 0.148 \pm 0.008$ dex and $\sigma_{bias} = 0.193 \pm 0.001$, but the bias does vary with cluster mass. The scatter in recovered masses can be attributed to both physical and numerical effects. The presence of any in-falling matter onto lower mass clusters can introduce a significant amount of substructure, leading to artificial biasing of the measured LOSVD to higher values, increasing the predicted mass (e.g., Ntampaka et al. 2015). Also, as the number of cluster galaxies decreases the LOSVD probability distribution function is poorly sampled leading to poorly recovered cluster masses due to numerical effects.

For the Targeted and Survey observations the power law predicted cluster masses give $\mu_{bias} = 0.135 \pm 0.003$ dex, $\sigma_{bias} = 0.370 \pm 0.002$ and $\mu_{bias} = 0.148 \pm 0.008$ dex, $\sigma_{bias} = 0.324 \pm 0.006$, respectively. So for the clusters that we detect with Survey observations, we obtain similar levels

of accuracy as to the Targeted observations, on the average. This does not mean that the Survey observations cannot be improved by Targeted observations. In fact, when comparing only the galaxies which overlap between the two samples the bias and scatter of the Targeted observations is significantly decreased as more cluster member galaxies are detected, better sampling the LOSVD probability distribution function. The Targeted observations perform similarly on the average because many lower mass clusters are included in the sample, increasing the bias of the overall sample.

In both Figures 5 and 6, we show the predicted (M_{pred}) versus true (M_{200c}) cluster masses for each of the two observing strategies. The lower panels show the fractional cluster mass error defined as:

$$\epsilon = (M_{pred} - M_{200c})/M_{200c} \tag{12}$$

where M_{pred} is the predicted cluster mass and M_{200c} is the true cluster mass. Higher values of ϵ indicate the predicted cluster mass exceeds the true cluster mass.

Qualitatively, the top panels of Figures 5 and 6 show that both the probability based and ML based methods out perform (closer to the black 1:1 relation) the power law method when taking advantage of other cluster observables (z, N_{gal}, etc.). Generally, we find that the single parameter probability and ML methods perform significantly poorer than the power law method, especially at low cluster masses. When combined with the cluster redshift, the predicted cluster masses are improved, because the range of cluster masses decrease with increasing redshift (see Figure 4). The final addition of the number of observed galaxies, N_{gal} acts as
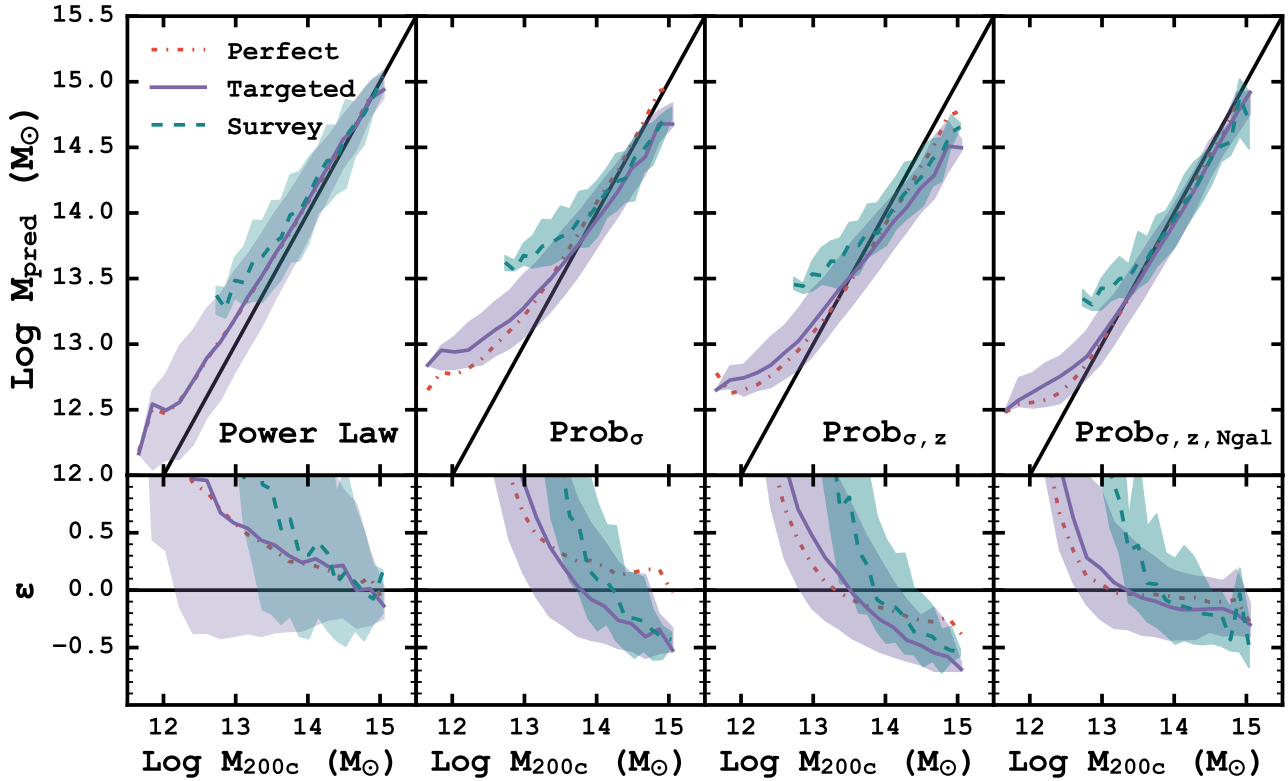
Figure 5. Mass predictions for the power law scaling relation (Equation 6) and the probability based technique with different input features as a function of true cluster mass. The bottom row of panels shows the fractional error (Equation 12) also as a function of true cluster mass. The solid black line shows the 1:1 relation. The orange, dash-dotted line is the median predicted mass for perfect observations. The solid, purple line is the median predicted mass for the Targeted observing, and the green, dashed line is the median recovered mass for the HETDEX-like observations. The shaded regions represent the 68% scatter around the median values.

a type of richness estimate, and significantly improves both the bias and the amount of scatter in the predicted masses.

We quantify the bias and scatter for all of the different cluster mass recovery strategies and observing methods in Table 1 and Table 2. It serves as a reference for future cluster observations with HETDEX. The columns represent bins of predicted galaxy cluster mass and the individual values show the bias and scatter of the true cluster mass. The three horizontal sections represent Perfect, Targeted and Survey observations respectively. So, for example, if a cluster mass is predicted using the $ML_{\sigma,z}$ method and Targeted observations to be $\mathrm{Log}\,M/M_\odot = 13 - 13.5$, it is biased upward by 0.03 ± 0.003 dex and has a scatter of 0.24 ± 0.009 dex.

A few caveats apply to the numbers given in Table 1 and Table 2. While we provide corrections for cluster masses above $10^{15}\,M_\odot$, they are estimated from only a handful of objects, and may not constitute a representative sample of clusters. This becomes particularly apparent for the probability methods with many features. As the number of observed features increases, the number of training clusters in any particular bin decreases. This leads to highly skewed biases and scatters for the high mass clusters and probability methods. We do not report any bin where such small number statistics dominate in Tables 1 and 2. On the opposite end of the cluster mass spectrum, there are very few, if any, clusters detected with Targeted or Survey observations be-

low $5 \times 10^{12}\,M_\odot$. Therefore, while we show these points in Figures 5 and 6, we exclude their biases and scatters from Tables 1 and 2 for the same reasons.

The method which produce the lowest scatter and bias depends on the mass of the cluster in question and the type of observations used. For the Targeted observations, the power law method outperforms all other methods, in terms of bias and scatter, for the highest mass clusters. But outside of the two highest mass bins, the $ML_{\sigma,z,N_{gal}}$ method shows the smallest amount of scatter and bias most consistently. With Survey observations, the power law again provides the lowest bias in the highest cluster mass bins, but is outperformed in terms of scatter by the other two methods. The $ML_{\sigma,z,N_{gal}}$ method shows the smallest amount of scatter and bias most consistently across the cluster mass range in question.

4.3 Impact of Training Sample Cosmology

All simulations (including that used for Buzzard) use specific values for cosmological parameters. When using simulation data to train ML methods, we incorporate all of those assumptions into the learned feature associations. One could imagine that the specific values of the cosmological parameters in the training sample could bias the ML results when applied to data (real or simulated) created from an unknown
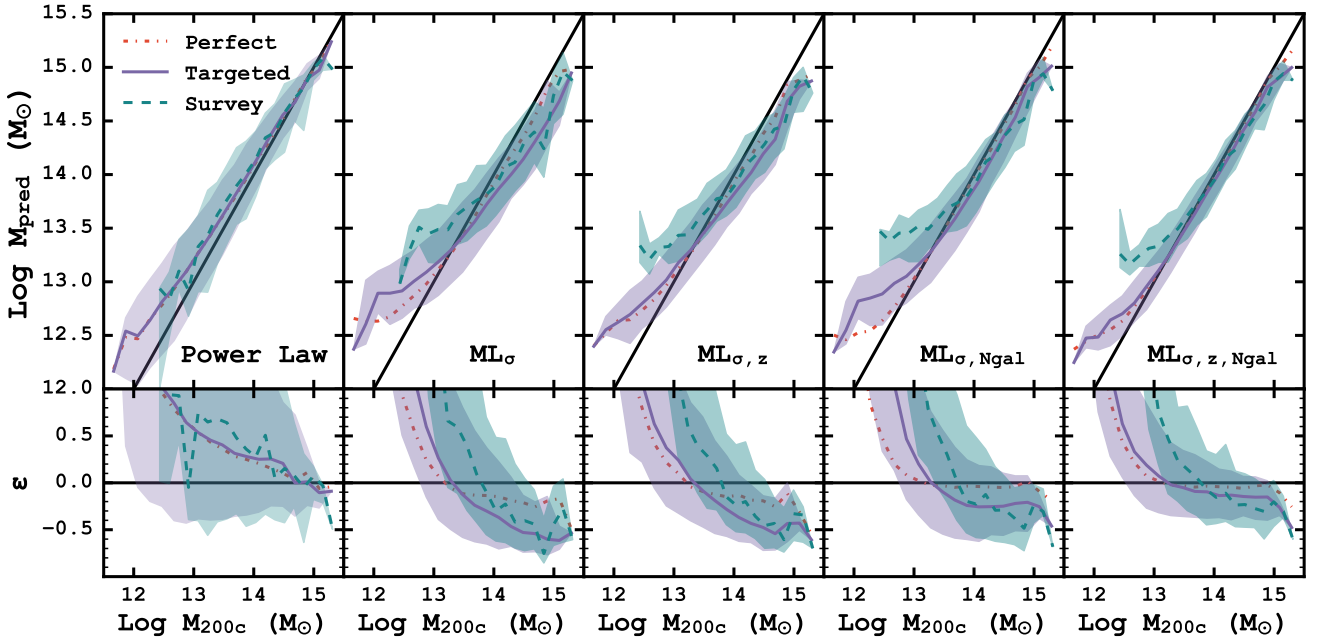
Figure 6. Mass predictions for the power law scaling relation (Equation 6) and the ML based technique with different input features as a function of true cluster mass. The bottom row of panels shows the fractional error (Equation 12) also as a function of true cluster mass. The solid black line shows the 1:1 relation. The orange, dash-dotted line is the median predicted mass for perfect observations. The solid, purple line is the median predicted mass for the Targeted observing, and the green, dashed line is the median recovered mass for the HETDEX-like observations. The shaded regions represent the 68% scatter around the median values.

true set of cosmological parameters. In addition, each simulation realizes galaxy populations in slightly different ways. The details of the simulation affect which galaxies are observed or not, and thus influences our ability to recover the desired cluster properties.

To test for this, we used the Millennium simulation (Springel et al. 2005) as an alternative data set. The Millennium simulation adopts a flat cosmological model based of the values derived from the Two-degree Field Galaxy Redshift Survey (Colless et al. 2001) and the first year data of the *Wilkinson Microwave Anisotropy Probe* (WMAP; Spergel et al. 2003): $\Omega_\Lambda = 0.75$, $\Omega_M = 0.25$, $\sigma_8 = 0.9$, $n_s = 1$ and $H_0 = 73$ km s^{-1}Mpc^{-1}. As this cosmology differs dramatically from that assumed in the Buzzard catalogs (see Section 2.1, the clusters in Millennium provide a testing sample to understand how a training sample derived from Buzzard will impact the mass recovery on a wholly new dataset.

We repeat our analysis using cluster halo and galaxy catalogs from the Millennium simulation obtained via querying the Millennium online database[3] (Lemson & The Virgo Consortium 2006). The Millennium simulation tracks 2160^3 dark matter particles of $8.6 \times 10^8\ h^{-1}$ M$_\odot$ inside a comoving $500\ (h^{-1}{\rm Mpc})^3$ box from $z = 127$ to 0. The following SQL query selects the cluster halos:

```
SELECT *
FROM    mfield..fof
WHERE   snapnum IN (SELECT snapnum
                    FROM    snapshots..mr
```

[3] http://gavo.mpa-garching.mpg.de/Millennium/

```
                    WHERE
z BETWEEN 0.01 AND 0.5)
        AND m_crit200 > 100
        AND random BETWEEN 0 AND 10000
```

To select the corresponding galaxies, we use:

```
SELECT sh.fofid,
       sh.subhaloid,
       g.galaxyid,
       g.x,
       g.y,
       g.z,
       g.redshift,
       g.velx,
       g.vely,
       g.velz,
       sdss.g_sdss,
       sdss.r_sdss,
       sdss.i_sdss
FROM    mfield..fofsubhalo AS sh
        INNER JOIN mpagalaxies..delucia2006a
            AS g
                ON sh.subhaloid = g.
                    subhaloid
        INNER JOIN mpagalaxies..
            delucia2006a_sdss2mass AS sdss
                ON g.galaxyid = sdss.
                    galaxyid
WHERE   sh.fofid IN (SELECT fofid
                FROM    mfield..fof
                WHERE   snapnum IN (SELECT
                    snapnum
```

Table 1. Mean bias (Eqn. 10) for different bins of predicted cluster mass. This table shows the bias in the predicted cluster mass for the perfect (top section), Targeted (middle section), and Survey (bottom section) observations in different predicted mass bins. The different mass recovery strategies are given in the leftmost column. It can be used to understand how the predicted cluster mass differs from the true cluster masses. Positive numbers indicate the predicted cluster mass over estimates when compared to the true cluster mass.

Method		$12.5-13$	$13-13.5$	$13.5-14$	$14-14.5$	$14.5-15$	$15-15.5$
				Bins – Log M_{pred}			
Power Law		0.23 ± 0.007	0.16 ± 0.003	0.11 ± 0.002	0.07 ± 0.004	0.02 ± 0.011	-0.07 ± 0.045
Prob	σ	0.32 ± 0.005	0.16 ± 0.003	0.10 ± 0.002	0.07 ± 0.004	0.05 ± 0.012	-0.18 ± 0.078
	σ, z	0.17 ± 0.005	0.01 ± 0.003	-0.06 ± 0.002	-0.11 ± 0.015	-0.14 ± 0.012	-0.38 ± 0.159
	σ, z, N_{gal}	0.04 ± 0.009	-0.02 ± 0.002	-0.02 ± 0.002	-0.05 ± 0.014	-0.22 ± 0.126	...
ML	σ	0.14 ± 0.006	-0.01 ± 0.003	-0.07 ± 0.003	-0.09 ± 0.005	-0.11 ± 0.014	-0.17 ± 0.090
	σ, z	0.12 ± 0.005	-0.01 ± 0.003	-0.06 ± 0.003	-0.08 ± 0.004	-0.11 ± 0.012	-0.24 ± 0.076
	σ, N_{gal}	0.04 ± 0.004	-0.02 ± 0.002	-0.02 ± 0.002	-0.02 ± 0.002	-0.02 ± 0.006	-0.08 ± 0.041
	σ, z, N_{gal}	0.04 ± 0.003	-0.02 ± 0.002	-0.02 ± 0.001	-0.02 ± 0.002	-0.02 ± 0.005	-0.08 ± 0.043

Perfect Observations (top section)

Method		$12.5-13$	$13-13.5$	$13.5-14$	$14-14.5$	$14.5-15$	$15-15.5$
Power Law		0.20 ± 0.008	0.13 ± 0.005	0.10 ± 0.005	0.09 ± 0.007	0.02 ± 0.014	-0.08 ± 0.043
Prob	σ	0.40 ± 0.005	0.17 ± 0.003	0.02 ± 0.004	-0.08 ± 0.006	-0.19 ± 0.015	-0.35 ± 0.122
	σ, z	0.25 ± 0.005	0.08 ± 0.003	-0.06 ± 0.003	-0.21 ± 0.015	-0.35 ± 0.016	-0.59 ± 0.145
	σ, z, N_{gal}	0.13 ± 0.004	0.01 ± 0.003	-0.05 ± 0.003	-0.12 ± 0.018	-0.44 ± 0.177	...
ML	σ	0.26 ± 0.006	0.02 ± 0.004	-0.13 ± 0.005	-0.24 ± 0.008	-0.35 ± 0.022	-0.39 ± 0.054
	σ, z	0.18 ± 0.005	0.03 ± 0.003	-0.10 ± 0.004	-0.21 ± 0.006	-0.31 ± 0.021	-0.33 ± 0.063
	σ, N_{gal}	0.22 ± 0.005	0.00 ± 0.004	-0.13 ± 0.004	-0.16 ± 0.007	-0.13 ± 0.014	-0.19 ± 0.059
	σ, z, N_{gal}	0.09 ± 0.004	-0.01 ± 0.002	-0.05 ± 0.002	-0.08 ± 0.004	-0.08 ± 0.010	-0.19 ± 0.060

Targeted Observations (middle section)

Method		$12.5-13$	$13-13.5$	$13.5-14$	$14-14.5$	$14.5-15$	$15-15.5$
Power Law		0.17 ± 0.068	0.17 ± 0.023	0.13 ± 0.014	0.07 ± 0.014	0.01 ± 0.022	-0.09 ± 0.062
Prob	σ	0.77 ± 0.030	0.42 ± 0.011	0.18 ± 0.008	-0.03 ± 0.009	-0.18 ± 0.017	-0.39 ± 0.102
	σ, z	0.61 ± 0.036	0.29 ± 0.012	0.08 ± 0.008	-0.11 ± 0.009	-0.38 ± 0.118	-0.48 ± 0.127
	σ, z, N_{gal}	0.48 ± 0.038	0.18 ± 0.011	0.02 ± 0.007	-0.08 ± 0.008	-0.50 ± 0.203	...
ML	σ	0.57 ± 0.046	0.24 ± 0.015	0.02 ± 0.012	-0.17 ± 0.013	-0.28 ± 0.027	-0.27 ± 0.117
	σ, z	0.48 ± 0.034	0.20 ± 0.013	0.03 ± 0.009	-0.13 ± 0.011	-0.26 ± 0.021	-0.31 ± 0.110
	σ, N_{gal}	0.55 ± 0.043	0.22 ± 0.013	0.00 ± 0.010	-0.14 ± 0.011	-0.22 ± 0.025	-0.19 ± 0.079
	σ, z, N_{gal}	0.42 ± 0.029	0.13 ± 0.011	-0.00 ± 0.007	-0.08 ± 0.008	-0.14 ± 0.016	-0.19 ± 0.079

Survey Observations (bottom section)

```
                           FROM
                                snapshots
                                ..mr
                           WHERE   z
                                BETWEEN
                                0.01 AND
                                0.5)
                           AND m_crit200 > 1000
                           AND random BETWEEN 0
                                AND 10000)
```

We select 4,806 clusters, comprised of 623,663 galaxies, at $0.02 < z < 0.5$ and $M > 10^{13}$ $M_\odot$, and apply the same data processing as with the Buzzard galaxies. We begin by assigning each galaxy an [O II] flux value (see Section 2.2), and "observe" each galaxy using realistic (see Section 2.4) observational limits. After recovering 3750 clusters which have at least five galaxies observed, we calculate the LOSVD of each cluster as in Section 3.2.

We conduct our test in two ways. Both use the ML methods (see Section 3.3.4) to predict the cluster masses of the Millennium clusters, but each test uses a different train-ing set. First, we use the full set of clusters detected in the Buzzard catalogs (14,000 clusters with $M > 10^{11}$ $M_\odot$) to train the ML. Second, the Millennium clusters are split into training-testing samples. This provides a test case where we have different cosmological choices between the training and testing samples, and the same cosmological assumptions in both samples. In addition, it provides two different treatments of galaxy evolution in cluster environments. The differing galaxy evolution effects can impact observed galaxy magnitude and color evolution. This provides an important check to understand whether the specific assumptions made in the models affect the results of this analysis.

The top panel of Figure 7 shows the ML predicted cluster masses for the ~4000 Millennium clusters as a function of true cluster mass. The orange (Millennium) and green (Buzzard) colors indicate the two different training samples. The median (solid and dashed lines) predicted cluster masses show similar trends regardless of the training data set used. The bottom panel of Figure 7 shows the fraction error (Equation 12) also as a function of true cluster mass. The large amount of scatter (the shaded area) in the fractional error for the Buzzard-trained predictions is due to the train-

Table 2. Mean scatter (Eqn. 11) in cluster mass after bias correction for different bins of predicted cluster mass. This table shows the scatter in the predicted cluster mass for the perfect (top section), Targeted (middle section), and Survey (bottom section) observations in different predicted mass bins. The different mass recovery strategies are given in the leftmost column. It can be used to understand how the predicted cluster mass differs from the true cluster masses.

	Method	12.5 − 13	13 − 13.5	13.5 − 14	14 − 14.5	14.5 − 15	15 − 15.5
				Bins – Log M_{pred}			
				Perfect Observations			
	Power Law	0.34 ± 0.005	0.22 ± 0.002	0.16 ± 0.002	0.14 ± 0.003	0.14 ± 0.008	0.11 ± 0.040
Prob	σ	0.26 ± 0.004	0.20 ± 0.002	0.16 ± 0.002	0.14 ± 0.003	0.16 ± 0.009	0.19 ± 0.071
Prob	σ, z	0.23 ± 0.003	0.19 ± 0.002	0.16 ± 0.002	0.55 ± 0.010	0.16 ± 0.009	0.39 ± 0.143
Prob	σ, z, N_{gal}	0.47 ± 0.007	0.14 ± 0.001	0.10 ± 0.001	0.54 ± 0.010	...	...
ML	σ	0.29 ± 0.004	0.24 ± 0.002	0.21 ± 0.002	0.19 ± 0.004	0.18 ± 0.010	0.22 ± 0.081
ML	σ, z	0.24 ± 0.003	0.20 ± 0.002	0.18 ± 0.002	0.16 ± 0.003	0.16 ± 0.009	0.19 ± 0.068
ML	σ, N_{gal}	0.19 ± 0.003	0.14 ± 0.001	0.10 ± 0.001	0.08 ± 0.002	0.07 ± 0.004	0.10 ± 0.037
ML	σ, z, N_{gal}	0.17 ± 0.002	0.13 ± 0.001	0.10 ± 0.001	0.07 ± 0.001	0.07 ± 0.004	0.11 ± 0.039
				Targeted Observations			
	Power Law	0.43 ± 0.006	0.39 ± 0.004	0.33 ± 0.004	0.27 ± 0.005	0.18 ± 0.010	0.11 ± 0.039
Prob	σ	0.24 ± 0.003	0.25 ± 0.002	0.25 ± 0.003	0.22 ± 0.004	0.19 ± 0.011	0.30 ± 0.110
Prob	σ, z	0.24 ± 0.003	0.24 ± 0.002	0.23 ± 0.002	0.56 ± 0.011	0.21 ± 0.012	0.36 ± 0.131
Prob	σ, z, N_{gal}	0.20 ± 0.003	0.19 ± 0.002	0.17 ± 0.002	0.67 ± 0.013	...	...
ML	σ	0.30 ± 0.004	0.32 ± 0.003	0.32 ± 0.003	0.30 ± 0.006	0.29 ± 0.016	0.13 ± 0.049
ML	σ, z	0.26 ± 0.004	0.25 ± 0.002	0.24 ± 0.003	0.23 ± 0.004	0.27 ± 0.015	0.16 ± 0.057
ML	σ, N_{gal}	0.27 ± 0.004	0.27 ± 0.003	0.27 ± 0.003	0.25 ± 0.005	0.18 ± 0.010	0.15 ± 0.053
ML	σ, z, N_{gal}	0.21 ± 0.003	0.18 ± 0.002	0.16 ± 0.002	0.14 ± 0.003	0.12 ± 0.007	0.15 ± 0.054
				Survey Observations			
	Power Law	0.40 ± 0.050	0.41 ± 0.016	0.38 ± 0.010	0.32 ± 0.010	0.25 ± 0.016	0.15 ± 0.056
Prob	σ	0.11 ± 0.024	0.18 ± 0.008	0.22 ± 0.006	0.22 ± 0.007	0.19 ± 0.012	0.25 ± 0.092
Prob	σ, z	0.13 ± 0.028	0.19 ± 0.008	0.22 ± 0.006	0.21 ± 0.007	1.31 ± 0.084	0.32 ± 0.115
Prob	σ, z, N_{gal}	0.14 ± 0.030	0.18 ± 0.008	0.19 ± 0.005	0.19 ± 0.006	...	...
ML	σ	0.27 ± 0.034	0.27 ± 0.011	0.31 ± 0.008	0.30 ± 0.009	0.30 ± 0.019	0.29 ± 0.106
ML	σ, z	0.20 ± 0.025	0.24 ± 0.009	0.24 ± 0.006	0.25 ± 0.008	0.24 ± 0.015	0.27 ± 0.100
ML	σ, N_{gal}	0.25 ± 0.032	0.23 ± 0.009	0.27 ± 0.007	0.26 ± 0.008	0.27 ± 0.018	0.20 ± 0.072
ML	σ, z, N_{gal}	0.17 ± 0.021	0.21 ± 0.008	0.20 ± 0.005	0.19 ± 0.006	0.17 ± 0.011	0.20 ± 0.071

ing set including clusters with masses below the $M = 10^{13}$ $M_\odot$ threshold for the Millennium clusters. This allows the ML method to predict masses which can be significantly different, whereas the Millennium training set does not include $M < 10^{13}$ $M_\odot$ clusters, which reduces the scatter of the predicted masses.

Based on these tests, the choice of cosmological parameters does not cause any significant offset in the predicted cluster masses from the trained ML methods. This highlights the versatility of our chosen ML method. The ML method could be further diversified by including cluster measurements from a wide range of cosmological simulations (or observations) which, in affect, marginalizes over all the cosmological assumptions further reducing the dependence.

5 HETDEX AS A GALAXY CLUSTER SURVEY AT $Z < 0.5$

5.1 Constraints on Cosmological Parameters

Galaxy clusters trace the peaks in the universal matter density, often referred to as the power spectrum of matter den-sity fluctuations or the matter power spectrum. This enables them to be sensitive probes of Ω_m, the total mass $(\Omega_b + \Omega_c)$ density, and σ_8, the normalization of the power spectrum. We constrain these parameters by the comparison of the number density of observed clusters to that predicted in cosmological models. Although, in reality, one measures $\sigma_8 \Omega_m^q$, where the value of q depends on the masses and redshifts of the halos considered.

To get a sense of how well observations of z < 0.5 galaxy clusters from HETDEX will be able to constrain cosmological parameters we follow the discussion of Weinberg et al. (2013) (hereafter W13), and begin with a few simplifying assumptions. While sensitive to Ω_m, the number density of clusters does not necessarily provide the strongest contraint, but combined with other data sets (e.g., CMB, BAO, supernovae, WL, etc.) it will constrain Ω_m to higher precision.

To estimate the error associated with a measurement of σ_8 (which W13 refer to as $\sigma_{11,abs}$), W13 consider two sources of uncertainty, the systematic uncertainties in cluster mass calibration and the statistical uncertainty in the observed number density of clusters. The authors combine these two
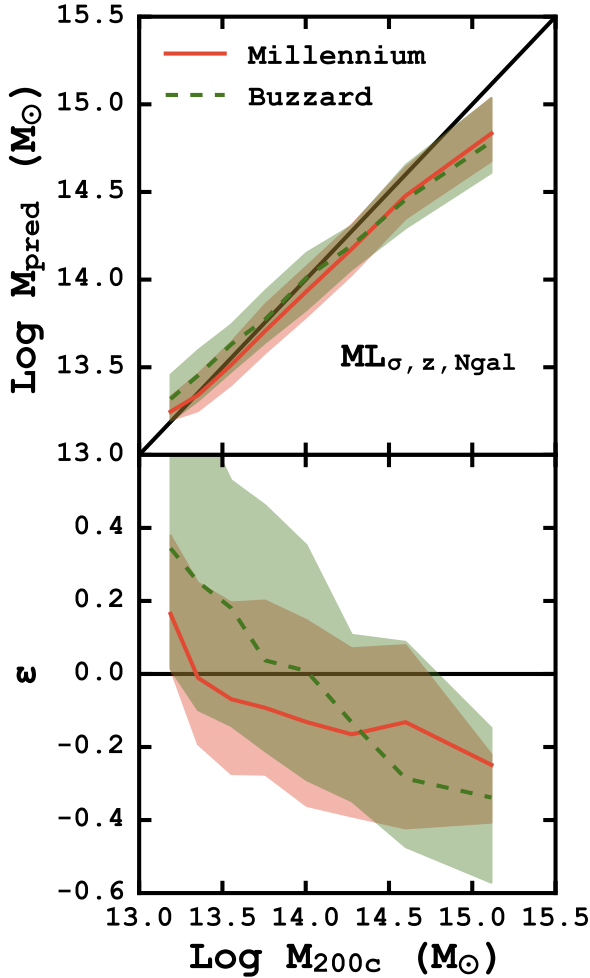
Figure 7. *Top:* ML based cluster mass predictions for the Millennium simulation clusters where the ML method has been trained with either a subset of the Millennium clusters (solid line) or the Buzzard catalog (dashed line). The shaded areas show the 68% scatter around the median. The solid black line shows the 1:1 relation. *Bottom:* The fractional error (Equation 12) also as a function of true cluster mass. The similarity of the predictions with the different training sets demonstrates how the ML method is not sensitive to the underlying cosmological assumptions.

uncertainties though (their Eq. 141):

$$\Delta \ln \sigma_8(z) \approx q(z) \times \max \left[\Delta \ln M, \alpha(z)^{-1} \Delta \ln N \right]. \quad (13)$$

where q is the degeneracy exponent between σ_8 and Ω_m, $\Delta \ln M$ is the mass scale uncertainty, $\Delta \ln N$ is the cluster statistical uncertainty, and α is slope of the cumulative HMF. Using the Tinker et al. (2008) HMF at $z \sim 0.2$ and a limiting cluster mass of 10^{14} M$_\odot$, W13 estimate $q \sim 0.4$, $\alpha \sim 3$, and find that any cluster survey with more than 10-20 clusters is dominated by the uncertainty in the overall mass scale.

For a survey such as HETDEX, we can estimate the constraints on σ_8 using Equation 13. If we consider clusters with masses above 10^{14} M$_\odot$ and with Perfect knowledge observations, the lowest mass scale uncertainty (given in Table 2) is $\Delta_{log_{10}} M \sim 0.075$ dex or about 20%. This gives a

uncertainty on σ_8 of 7%. For clusters above 10^{14} M$_\odot$, Survey observations constrain the masses to about 51% which, in turn, constrains σ_8 to 20%.

Because of the simplifying assumptions, and the superior quality of the data (no contamination, signal-to-noise issues, etc.), realistic expectations for HETDEX is to directly constrain σ_8 is not yet competitive with other methods (e.g., CMB, WL, X-ray). For example, de Haan et al. (2016) constrain σ_8 to $\sim$ 5% using a sample of 337 SZE detected clusters from the SPT-SZE survey.

We can use the rule-of-thumb calculations given in W13 (Equations 154–155) to estimate the uncertainties required in both the absolute cluster mass scale and the intrinsic scatter to keep a cosmological analysis limited by cluster statistics. For the $\sim$ 670 clusters, with masses above 10^{14} M$_\odot$, detected with Survey observations to constrain σ_8 and to be dominated by cluster statistics alone ($\Delta \ln N \sim N^{-1/2}$), the error on the absolute cluster calibration would need to be better than 1.3%. For a fully Targeted survey, about 1600 clusters with masses above 10^{14} M$_\odot$, this cluster mass calibration uncertainty reduces to $< 1\%$. Similarly, the uncertainty associate with the scatter must be approximately 2.2% and 1.4% for Survey and Targeted observations respectively, after assuming an intrinsic scatter of 20%. Comparing these estimates to the uncertainties associated with the Targeted and Survey observations, we are dominated by the uncertainty associated with the absolute cluster mass scale calibration. Nevertheless, while analysis of HETDEX clusters may not provide the most accurate constraint on σ_8, it will provide important systematics checks on other studies and will ultimately improve the measurements of σ_8.

5.2 Scale and Scatter of the Richness-Cluster Mass Relation

Large-scale optical surveys (e.g., DES and LSST) expect to detect hundreds of thousands of galaxy clusters at $z < 1$. Because they produce photometry only, a major challenge for these surveys is relating a cluster observable to the total DM mass. One promising cluster mass estimator is the optical richness (e.g., Abell 1958). Specifically, here, we use as the richness, λ, which is the weighted number of galaxies within a scale aperture (e.g., Rozo et al. 2011) as calculated by the redMaPPer algorithm (Rykoff et al. 2012). Previous works (e.g., Rozo et al. 2010) show that the richness correlates strongly with cluster mass on the average, but the absolute mass scale of the optical richness mass estimator and the scatter in cluster mass at fixed optical richness are imprecisely known (Rykoff et al. 2012). These systematics remain the major source of uncertainty in deriving cosmological constraints from cluster abundances and must be measured using independent methods to realize the full potential of these types of surveys.

One of the main goals of this study is to understand how well HETDEX will be able to measure the scatter in the richness–mass relationship. To this end, we choose to impose a richness–mass relation onto the clusters in the Buzzard catalogs. The true richness–mass relation could depend strongly on the number and types of environmental effects, because such effects have a strong impact on the number and types of galaxies observed in clusters (e.g., Gunn & Gott, J. Richard 1972; Balogh et al. 2000; White et al. 2010). Any

environmental effects included in Buzzard could potentially impact our observed richness. The imposition of an empirical richness–mass relation ensures the richness values correspond correctly to the clusters in our sample, could provide direct observational tests in the future.

We generate richnesses based on the true cluster masses, and for testing, we assume two versions of the richness–mass relationship. Farahi et al. (2016) base the relation on stacked velocity dispersions, and Simet et al. (2016) use weak lensing measurements to construct their relation. Because we are investigating HETDEX's ability to recover the overall cluster mass scale and underlying scatter in the mass-richness relationship, we use the true cluster masses perturbed by a known amount to estimate the observed richness.

To confirm that measuring the underlying scatter is possible, after generating richness values we calculate the scatter of the cluster masses at fixed λ, $\sigma_{M|\lambda}$, by comparing the true, unperturbed cluster masses against the richness. We do recover the expected scatter, often, to well within 0.01 dex. We repeat the process with both assumed richness–mass relationships and recover the expected scatter in both instances.

We use the lambda values generated above in combination with the $M_{\sigma,z,N_{gal}}$ predicted cluster mass which have been bias corrected using the values in Table 1 and denoted $M_{pred,corr}$. The use of biased cluster mass predictions inhibits our ability to accurately recover any scatter in richness–mass relationship, and is discussed further below.

Primarily, we are interested in the intrinsic scatter of the richness–mass relationship. This is because HETDEX is uniquely situated to estimate the scatter, whereas studies relying on stacked data (e.g., Farahi et al. 2016; Simet et al. 2016) lose that information. We begin by attempting to constrain the absolute mass scale, and as part of our fitting process, we estimate the overall scatter in the relationship. In order to understand how HETDEX will constrain the absolute mass scale, we find the best fitting relation to our richness–mass data. To generate the best fitting lines, we follow the general procedure of Hogg et al. (2010), by defining an objective function and then minimizing the loss. Our objective function is

$$P(y_i|x_i,\sigma_{yi},m,b,\sigma) = \frac{1}{\sqrt{2\,\pi\,(\sigma_{yi}^2+\sigma^2)}}\,\exp\left(-\frac{[y_i-m\,x_i-b]^2}{2\,(\sigma_{yi}^2+\sigma^2)}\right)$$
(14)

where y_i is the observed cluster mass, x_i is the observed richness, σ_{yi} is the uncertainty in observed cluster mass, m is the power law slope, b is the overall cluster mass scale, and σ is the intrinsic scatter between richness and cluster mass. We assume that the intrinsic scatter is constant from point to point and that all of the measurement errors are Gaussian. We convert this objective function into a likelihood by taking the product of all the individual probabilities:

$$\mathscr{L} = \prod_{i=1}^{N} P(y_i|x_i,\sigma_{yi},m,b,\sigma).$$
(15)

We again rely on MCMC samples to sample the posterior probability distribution and thus maximize the likelihood. The best fitting slope and intercept are quoted as the median value of the posterior probability distribution with 68% error

bars defined as the square root of the second moment of the same distribution.

We limit our clusters to those with $10 \leq \lambda < 130$ in our fitting analysis because above $\lambda = 130$ there are too few clusters and number-counting errors dominate. Other observational studies (e.g., Saro et al. 2015) which have lower limits on λ, so we exclude anything less than $\lambda = 10$. For a richness–mass relation with an intrinsic scatter of $\langle\sigma_{M|\lambda}\rangle = 0.25$ dex, we find a best-fitting relation for the Targeted observations as

$$\log\ M_{200c}/M_{\odot} = 12.46 \pm 0.02 + 1.07 \pm 0.02\ \log\ \lambda$$
(16)

and the Survey observations as

$$\log\ M_{200c}/M_{\odot} = 12.64 \pm 0.05 + 0.98 \pm 0.03\ \log\ \lambda$$
(17)

This gives $M_{200c} = (1.45 \pm 0.12) \times 10^{14}\ M_{\odot}$ and $M_{200c} = (1.59\pm0.27)\times10^{14}\ M_{\odot}$ at $\lambda = 40$ for the Targeted and Survey observations respectively. In both cases, this normalization differs significantly from the $M_{200c} \approx 2.1 \times 10^{14} h^{-1}\ M_{\odot}$ found in recent work Li et al. (2016); Simet et al. (2016). If the intrinsic scatter is reduced to ~ 0.05 dex we recover an overall normalization of $M_{200c} = (2.14\pm0.12)\times10^{14}\ M_{\odot}$ and $M_{200c} = (2.10 \pm 0.26) \times 10^{14}$ for the Targeted and Survey observations at $\lambda = 40$.

We also estimate the intrinsic scatter. For observations with a richness–mass relation intrinsic scatter of $\langle\sigma_{M|\lambda}\rangle = 0.25$ dex, we recover $\langle\sigma_{M|\lambda}\rangle = 0.236 \pm 0.003$ dex and $\langle\sigma_{M|\lambda}\rangle = 0.257 \pm 0.007$ dex for the Targeted and Survey observations respectively.

Figure 8 summarizes the main results of this investigation. The top panel shows the generated optical richness, λ, versus the predicted cluster mass. The cluster masses are the $ML_{\sigma,z,N_{gal}}$ based and correspond to the Targeted and Survey observation strategies. The bottom panel of Figure 8 shows the scatter in the predicted cluster masses at fixed richness, $\sigma_{M|\lambda}$. The solid line represents the intrinsic amount of scatter added to the masses. The cluster masses are binned in increasing ten richness intervals ($10 - 20$, $20 - 30$, etc.). The inset upper panel shows the intrinsic scatter versus the recovered average scatter at fixed richness, $\langle\sigma_{M|\lambda}\rangle$ and illustrates how well the two observation strategies recover the intrinsic scatter.

We find that we are able to accurately recover an average intrinsic scatter of $0.2 < \langle\sigma_{M|\lambda}\rangle < 0.3$ dex, finding $\langle\sigma_{M|\lambda}\rangle = 0.257 \pm 0.007$ at $\sigma_{true} = 0.25$ with Survey observations. As the intrinsic scatter increases or decreases, we fail to recover the scatter as accurately.

For the richness range $10 \leq \lambda < 130$ the intrinsic scatter in between the $M_{pred,corr}$ predicted cluster masses and the true cluster mass (the basis of our richnesses) is ~ 0.15 dex for Targeted observations and ~ 0.20 dex for Survey observations. As we reduce the overall scatter in our cluster mass recovery, this floor will lower. We underestimate the scatter in high intrinsic scatter relations because any residual bias remaining in the predicted clusters masses after correction reduces the observed scatter. Because the bias subtraction when creating $M_{pred,corr}$ subtracts the mean bias, we are left with a small amount of residual bias, lowering the measured scatter for high scatter relationships.
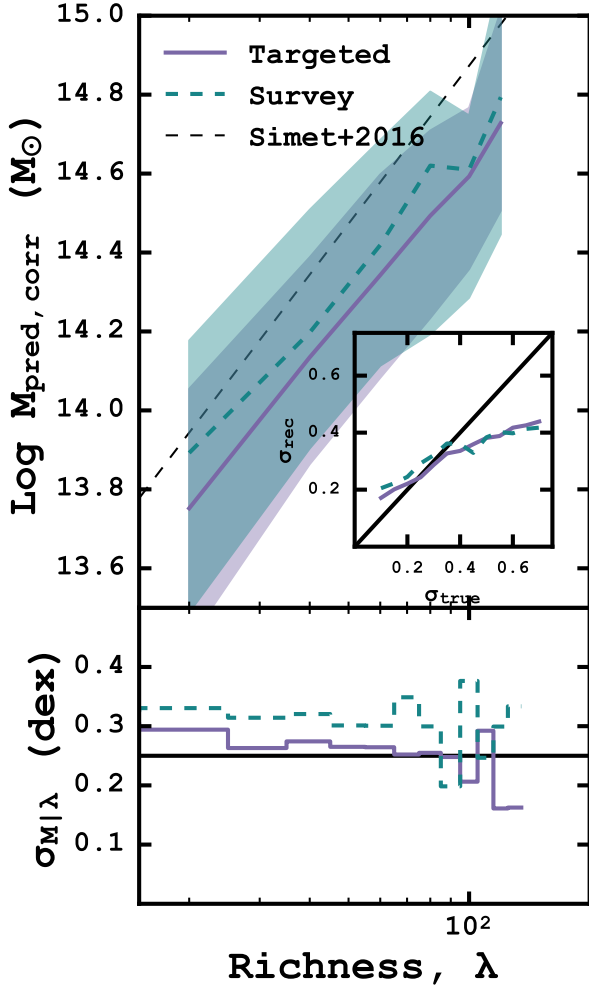
Figure 8. *Top*: The optical richness, λ, versus the corrected predicted cluster mass. The solid, purple line is the median predicted mass for the Targeted observing, and the turquoise, dashed line is the median recovered mass for the HETDEX-like observations. The shaded regions represent the 68% scatter around the median values. *Bottom*: The scatter in the relation at fixed richness. The solid black line shows the intrinsic scatter of $\sigma_{true} = 0.25$ dex. Color coding is the same as the top panel. *Inset*: The evolution of the intrinsic scatter versus the average recovered scatter, σ_{rec}.

6 SUMMARY

Here, we present detailed simulations of the upcoming HETDEX survey's applicability to the detection and total mass measurement of galaxy clusters based on emission line and continuum redshifts for galaxies at z < 0.5. Using mock galaxy catalogs and simple HETDEX-like observational strategies and limits, we observe our simulated sky, estimate the number of clusters observed, and derive basic cluster parameters, redshift, line-of-sight velocity dispersion (LOSVD). Using a traditional power law-based, velocity dispersion, scaling relation along with more advanced probability and machine learning (ML) techniques, we estimate the total mass for each cluster. We discuss each cluster mass estimate's precision, and discuss the ability of HETDEX to constrain the cosmological parameter σ_8 based on

those predicted cluster masses. In addition, we comment on how HETDEX may improve current and future photometric large-area sky surveys' cluster mass estimates derived from optical richness.

Our main conclusions are the following:

(i) After considering the observational limits of HETDEX, we find 14,189 clusters with at least five cluster members in the HETDEX survey volume. Of those, 1,760 clusters are detected with HETDEX-like survey observations, with the majority of failed recoveries due to the HETDEX tiling pattern. The number of cluster members recovered with Survey observations is almost exactly 4.5 times fewer than a fully Targeted survey, across both a wide range of redshifts and cluster masses.

(ii) We find a traditional power law conversion from LOSVD to cluster mass predicts the true cluster mass with little bias or scatter for clusters Log $M/M_\odot = 14.5$ and above. Below this mass the bias and scatter rapidly increases. In contrast, the probability based and ML based cluster mass estimators are able to predict cluster mass with similar or smaller scatter across all cluster masses. The scatter further decreases when the probability based and ML estimators are combined with other cluster observables besides the LOSVD. For HETDEX-like observations and clusters with $13 < \mathrm{Log}\,M/M_\odot < 14.5$, we find the $\mathrm{ML}_{\sigma,z,N_{gal}}$ method results in the smallest scatter. Below Log $M/M_\odot = 13$ no method with Survey observations gives a bias of less than 50%. For the highest mass clusters the power law method gives the lowest bias and scatter. In short, no single method is superior in all regards. The technique should be chosen to minimize the desired systematic, but we find $\mathrm{ML}_{\sigma,z,N_{gal}}$ provides the best performance across the large range of cluster masses, and observation strategies.

(iii) In general, we find that the measured scatter of cluster masses decreases when considering Targeted versus Survey observations. Clusters at all masses can benefit from targeted follow-up observations, although the accuracy gain will be smaller than can be achieved from cluster mass prediction method changes. Targeted follow-up observations reduces the measured scatter by $\sim 10\%$ when comparing like recovery methods.

(iv) The $\sim 51\%$ cluster mass accuracy of Survey observations places approximately a 20% constraint on σ_8. This can be tightened to approximately 12% with follow-up targeted observations. Most importantly, the observations from HETDEX will provide systematics checks on other studies, ultimately improving all future measurements of σ_8

(v) HETDEX will be able to place important, independent constraints on the amount of scatter in the optical richness–mass relationship. It will to a less extent constrain the overall normalization of the relation. This should provide an important tool in the calibration of large-area sky surveys which rely on photometric data only to estimate cluster masses.

It is the author's hope that this work may be useful to others when conducting their own research. Because this work relies heavily on (often) complex data analysis, and in order to promote transparency and reproducible science, we provide all of the code used to conduct this study at https://github.com/boada/HETDEXCluster. Regrettably, large file size prevents including the source data

with the analysis routines. The authors are happy to provide them, if requested.

ACKNOWLEDGEMENTS

REFERENCES

Abell, G. O. 1958, The Astrophysical Journal Supplement Series, 3, 211

Acquaviva, V. 2016, Monthly Notices of the Royal Astronomical Society, 456, 1618

Acquaviva, V., Gawiser, E., Leung, A. S., & Martin, M. R. 2014, Proceedings of the International Astronomical Union, 10, 365

Alam, S., Albareti, F. D., Prieto, C. A., et al. 2015, The Astrophysical Journal Supplement Series, 219, 12

Balogh, M. L., Navarro, J. F., & Morris, S. L. 2000, The Astrophysical Journal, 540, 113

Baxter, E. J., Rozo, E., Jain, B., Rykoff, E., & Wechsler, R. H. 2016, eprint arXiv:1604.00048, 7

Beers, T. C., Flynn, K., & Gebhardt, K. 1990, The Astronomical Journal, 100, 32

Behroozi, P. S., Wechsler, R. H., & Wu, H.-Y. 2013, The Astrophysical Journal, 762, 109

Bocquet, S., Saro, A., Mohr, J. J., et al. 2015, The Astrophysical Journal, 799, 214

Carlstrom, J. E., Holder, G. P., & Reese, E. D. 2002, Annual Review of Astronomy and Astrophysics, 40, 643

Carlstrom, J. E., Ade, P. A. R., Aird, K. A., et al. 2011, Publications of the Astronomical Society of the Pacific, 123, 568

Caruana, R., & Niculescu-Mizil, A. 2006, in Proceedings of the 23rd international conference on Machine learning - ICML '06, ACM (New York, New York, USA: ACM Press), 161–168

Chabrier, G. 2003, Publications of the Astronomical Society of the Pacific, 115, 763

Colless, M., Dalton, G., Maddox, S., et al. 2001, Monthly Notices of the Royal Astronomical Society, 328, 1039

Crocce, M., Pueblas, S., & Scoccimarro, R. 2006, Monthly Notices of the Royal Astronomical Society, 373, 369

de Haan, T., Benson, B. A., Bleem, L. E., et al. 2016, eprint arXiv:1603.06522, arXiv:1603.06522

Eisenstein, D. J., Zehavi, I., Hogg, D. W., et al. 2005, The Astrophysical Journal, 633, 560

Evrard, A. E., Bialek, J., Busha, M., et al. 2008, The Astrophysical Journal, 672, 122

Faltenbacher, A., & Diemand, J. 2006, Monthly Notices of the Royal Astronomical Society, 369, 1698

Farahi, A., Evrard, A. E., Rozo, E., Rykoff, E. S., & Wechsler, R. H. 2016, eprint arXiv:1601.05773, arXiv:1601.05773

Foreman-Mackey, D., Hogg, D. W., Lang, D., & Goodman, J. 2013, Publications of the Astronomical Society of the Pacific, 125, 306

Goodman, J., & Weare, J. 2010, Communications in Applied Mathematics and Computational Science, 5, 65

Gunn, J. E., & Gott, J. Richard, I. 1972, The Astrophysical Journal, 176, 1

Hill, G. J., Gebhardt, K., Komatsu, E., et al. 2008, Panoramic Views of Galaxy Formation and Evolution ASP Conference Series, 399

Hill, G. J. G., Tuttle, S. S. E., Lee, H., et al. 2012, in Proceedings of the SPIE, Vol. 8446, Ground-based and Airborne Instrumentation for Astronomy IV, ed. I. S. McLean, S. K. Ramsay, & H. Takami, 84460N

Hilton, M., & Boada, S. 2016, Astrophysics Source Code Library, record ascl:1607.016

Hogg, D. 1999, arXiv preprint astro-ph/9905116, 1, 1

Hogg, D. W., Bovy, J., & Lang, D. 2010, eprint arXiv:1008.4686, arXiv:1008.4686

Hunter, J. D. 2007, Computing in Science & Engineering, 9, 90

Kelz, A., Jahn, T., Haynes, D., et al. 2014, in Proceedings of the SPIE, ed. S. K. Ramsay, I. S. McLean, & H. Takami, Vol. 9147, 914775

Kirk, B., Hilton, M., Cress, C., et al. 2015, Monthly Notices of the Royal Astronomical Society, 449, 4010

Lemson, G., & The Virgo Consortium. 2006, eprint arXiv:astro-ph/0608019, arXiv:0608019

Li, R., Shan, H., Kneib, J.-P., et al. 2016, Monthly Notices of the Royal Astronomical Society, 458, 2573

LSST Dark Energy Science Collaboration. 2012, arXiv preprint arXiv:1211.0310, 133

Mantz, A., Allen, S. W., Rapetti, D., & Ebeling, H. 2010, Monthly Notices of the Royal Astronomical Society, 406, no

Mantz, A. B., Allen, S. W., Morris, R. G., et al. 2015, Monthly Notices of the Royal Astronomical Society, 449, 199

—. 2016, eprint arXiv:1606.03407, 19, 1

Meinshausen, N. 2006, J. Mach. Learn. Res., 7, 983

Milvang-Jensen, B., Noll, S., Halliday, C., et al. 2008, Astronomy & Astrophysics, 482, 419

Munari, E., Biviano, A., Borgani, S., Murante, G., & Fabjan, D. 2013, Monthly Notices of the Royal Astronomical Society, 430, 2638

Murray, S., Power, C., & Robotham, A. 2013, Astronomy and Computing, 3-4, 23

Neal, R. M. 1997, Markov Chain Monte Carlo Methods Based on 'Slicing' the Density Function, Tech. Rep. 9722, Department of Statistics, University of Toronto, Toronto, doi:10.1.1.48.886

Ntampaka, M., Trac, H., Sutherland, D. J., et al. 2015, The Astrophysical Journal, 803, 50

—. 2016, The Astrophysical Journal, 831, 135

Oke, J. B. 1974, The Astrophysical Journal Supplement Series, 27, 21

Old, L., Skibba, R. A., Pearce, F. R., et al. 2014, Monthly Notices of the Royal Astronomical Society, 441, 1513

Old, L., Wojtak, R., Mamon, G. A., et al. 2015, Monthly Notices of the Royal Astronomical Society, 449, 1897

Pearson, R. J., Ponman, T. J., Norberg, P., Robotham, A. S. G., & Farr, W. M. 2015, Monthly Notices of the Royal Astronomical Society, 449, 3082

Pedregosa, F., Varoquaux, G., Gramfort, A., et al. 2012, Journal of Machine Learning Research, 12, 2825

Perez, F., & Granger, B. E. 2007, Computing in Science & Engineering, 9, 21

Pipino, A., & Pierpaoli, E. 2010, Monthly Notices of the Royal Astronomical Society, 404, 16

Planck Collaboration. 2013, Astronomy & Astrophysics, 571, 19

Reddick, R. M., Wechsler, R. H., Tinker, J. L., & Behroozi, P. S. 2013, The Astrophysical Journal, 771, 30

Ripley, B. D. 2007, Pattern recognition and neural networks (Oxford, UK: Cambridge University Press), 416

Robotham, A. S. G., Norberg, P., Driver, S. P., et al. 2011, Monthly Notices of the Royal Astronomical Society, 416, 2640

Rozo, E., Wu, H.-Y., & Schmidt, F. 2011, The Astrophysical Journal, 735, 118

Rozo, E., Wechsler, R. H., Rykoff, E. S., et al. 2010, The Astrophysical Journal, 708, 645

Ruel, J., Bazin, G., Bayliss, M., et al. 2014, The Astrophysical Journal, 792, 45

Rykoff, E. S., Koester, B. P., Rozo, E., et al. 2012, The Astrophysical Journal, 746, 178

Rykoff, E. S., Rozo, E., Busha, M. T., et al. 2014, The Astrophysical Journal, 785, 104

Saro, A., Mohr, J. J., Bazin, G., & Dolag, K. 2013, The Astrophysical Journal, 772, 47

Saro, A., Bocquet, S., Rozo, E., et al. 2015, Monthly Notices of the Royal Astronomical Society, 454, 2305

Sehgal, N., Trac, H., Acquaviva, V., et al. 2011, The Astrophysical Journal, 732, 44

Sifón, C., Hoekstra, H., Cacciato, M., et al. 2015, Astronomy & Astrophysics, 575, A48

Sifón, C., Menanteau, F., Hasselfield, M., et al. 2013, The Astrophysical Journal, 772, 25

Sifón, C., Battaglia, N., Hasselfield, M., et al. 2016, Monthly Notices of the Royal Astronomical Society, 461, 248

Simet, M., McClintock, T., Mandelbaum, R., et al. 2016, eprint arXiv:1603.06953, arXiv:1603.06953

Spergel, D. N., Verde, L., Peiris, H. V., et al. 2003, The Astrophysical Journal Supplement Series, 148, 175

Springel, V. 2005, Monthly Notices of the Royal Astronomical Society, 364, 1105

Springel, V., White, S. D. M., Jenkins, A., et al. 2005, Nature, 435, 629

Sunyaev, R. A., & Zeldovich, Y. B. 1972, Comments on Astrophysics and Space Physics, 4

Swetz, D. S., Ade, P. A. R., Amiri, M., et al. 2011, The Astrophysical Journal Supplement Series, 194, 41

The Dark Energy Survey Collaboration. 2005, eprint arXiv:astro-ph/0510346, 42

Tin Kam Ho. 1995, in Proceedings of 3rd International Conference on Document Analysis and Recognition, Vol. 1, IEEE (IEEE Comput. Soc. Press), 278–282

Tin Kam Ho. 1998, IEEE Transactions on Pattern Analysis and Machine Intelligence, 20, 832

Tinker, J., Kravtsov, A. V., Klypin, A., et al. 2008, The Astrophysical Journal, 688, 709

van der Burg, R. F. J., Muzzin, A., Hoekstra, H., et al. 2014, Astronomy & Astrophysics, 561, A79

Vanderlinde, K., Crawford, T. M., de Haan, T., et al. 2010, The Astrophysical Journal, 722, 1180

Walker, M. G., Mateo, M., Olszewski, E. W., et al. 2006, The Astronomical Journal, 131, 2114

Weinberg, D. H., Mortonson, M. J., Eisenstein, D. J., et al. 2013, Physics Reports, 530, 87

White, M., Cohn, J. D., & Smit, R. 2010, Monthly Notices of the Royal Astronomical Society, 408, 1818

Xu, X., Ho, S., Trac, H., et al. 2013, The Astrophysical Journal, 772, 147

This paper has been typeset from a T_EX/L^AT_EX file prepared by the author.